Baku State University: Journal of Physics & Space Sciences, **2026**, v3 (1), p. 33-48

journal homepage: http://bsuj.bsu.edu.az/en

Mixed-halide perovskites for optoelectronics: a comparative study of $CH_3NH_3PbICl_2$ and $CH_3NH_3SnICl_2$ thin films

Sevinj G. Nuriyeva*[1], Maarif A. Jafarov[2], Aynura H. Karimova[3], Fidan I. Novruzlu[2]

[1]Nano Research Laboratory, Center of Excellence in Research, Development and Innovation,
Baku State University, Baku, Azerbaijan;
[2]Department of Chemical Physics of the Nanomaterials, Baku State University, Baku, Azerbaijan;
[3]Department Chemistry of High Molecular Weight Compounds, Baku State University,
Baku, Azerbaijan

Received 20-Dec-2025; Accepted 03-Feb-2026
DOI: https://doi.org/10.30546/209501.101.2026.3.01.309

Abstract

In this study, mixed-halide perovskite thin films of methylammonium lead iodide chloride ($CH_3NH_3PbICl_2$) and methylammonium tin iodide chloride ($CH_3NH_3SnICl_2$) were fabricated using the doctor-blade coating technique and systematically investigated to evaluate the influence of partial chloride incorporation on their structural and optical properties. X-ray diffraction (XRD) and atomic force microscopy (AFM) analyses confirmed improved crystallinity and increased grain size in both materials. $CH_3NH_3SnICl_2$ films exhibited smoother surface morphology and higher phase purity, while $CH_3NH_3PbICl_2$ showed minor secondary phases such as PbI_2 and $PbCl_2$. Fourier-transform infrared (FTIR) spectra revealed characteristic vibrational modes of the methylammonium ($CH_3NH_3^+$) cation, with slight shifts indicating lattice modifications due to Cl^- substitution. UV–Vis absorption spectra showed absorption edges near 760 nm ($E_g \approx 1.54$ eV) and 830 nm ($E_g \approx 1.55$ eV) for $CH_3NH_3PbICl_2$ and $CH_3NH_3SnICl_2$, respectively. Photoluminescence spectra exhibited strong emissions at ~750 nm and ~820 nm, suggesting reduced defect density and efficient radiative recombination. These findings highlight mixed-halide perovskites as promising materials for stable optoelectronic applications.

Keywords: Hybrid perovskites; mixed-halide perovskites; $CH_3NH_3PbICl_2$; $CH_3NH_3SnICl_2$; structural characterization; band gap tuning; optical properties.
PACS Numbers: 61.66.Hq; 78.20.-e; 78.55.-m; 73.50.Pz; 88.40.H

Corresponding author – Tel.: (+994) 50 257 71 87
e-mail adress: snuriyeva@bsu.edu.az; *ORCID ID*: 0000-0003-0331-6556

1. Introduction

The increasing global demand for clean and sustainable energy has stimulated intensive research into novel photovoltaic materials, among which organometal halide perovskites have emerged as promising candidates due to their superior optoelectronic properties, tunable direct band gaps, and high absorption coefficients [1-3]. Even thin films (with thicknesses 300-500 nm) can offer excellent light harvesting, making these compounds particularly attractive for lightweight and flexible photovoltaic devices. Modifying the halide composition (I^-, Br^-, Cl^-) enables precise their band gap tuning, making them suitable for application in photodetectors, light-emitting diodes (LEDs), lasers, and other optoelectronic platforms [4-6].

Micro- and nano-sized perovskites differ substantially in synthesis conditions, such as precursor concentrations, nucleation and growth mechanisms, stabilization strategies, and thermal treatment regimes. Nanostructured perovskites demonstrate size- and morphology-dependent optical tunability, while microcrystalline thin films show long-term structural and optical stability, making both techniques valuable in photovoltaic and photonic technologies [7-9].

Within this class of materials, hybrid organic-inorganic perovskites based on the methylammonium cation are of especially importance. Lead and tin-based perovskites, such as $CH_3NH_3PbX_3$ and $CH_3NH_3SnX_3$ (X=I, Br, Cl) and their mixed-halide derivatives, exhibit highly ordered crystal lattices and advantageous synthesis at extremely mild conditions [10-11]. However, their long-term stability remains a challenge, as pure iodide or chloride phases are prone to degradation due to moisture, oxygen, and temperature variations.

To overcome these limitations, mixed-halide perovskites have attracted considerable interest. Partial incorporation of iodide with chloride in lead-based perovskites (e.g., $CH_3NH_3PbICl_2$) improves structural stability, film morphology, increases absorption edges, and decreases defect density [12-13]. In comparison with their single-halide analogues, mixed-halide systems exhibit stronger photoluminescence, improved crystallinity, and higher phase stability, and developed resistance to environmental degradation which are significant for optoelectronic and photovoltaic devices [6, 14].

Related stabilization strategies have been improved to tin-based systems, such as $CH_3NH_3SnICl_2$. While $CH_3NH_3SnI_3$ exhibits a narrow band gap (Eg≈1.3 eV) and strong light absorption in the visible-near-infrared region, but prone to rapid degradation due to the facile oxidation of Sn^{2+} to Sn^{4+}. Incorporation of chloride into the tin-iodide lattice partially reduces this oxidation, yielding $CH_3NH_3SnICl_2$ with enhanced crystallinity, smoother film morphology, and increased optical response [15, 16]. Previously reported optical studies show that Sn-based mixed-halide perovskites display wide band gaps (Eg≈2.6-2.8 eV) and visible-range emission peaks, demonstrating the strong effect of halide substitution on structural and electronic properties. However, the performance of $CH_3NH_3SnICl_2$ remain highly sensitive on synthesis conditions, including solvent composition, precursor ratios, and annealing temperature, which determine film stability and reproducibility [17].

In this context, a direct comparative investigation of $CH_3NH_3PbICl_2$ and $CH_3NH_3SnICl_2$ is crucial for understanding the structural, optical, and morphological features of mixed-halide perovskites. Such analysis not only defines the role of partial chloride incorporation in stabilizing hybrid perovskite lattices but also provides insights into their potential as functional materials for photovoltaic and optoelectronic applications.

The present work aims to provide a comprehensive comparative analysis of $CH_3NH_3PbICl_2$ and $CH_3NH_3SnICl_2$ hybrid perovskites, focusing on their structural and optical characteristics. By correlating partial iodide- chloride substitution with changes in crystallinity, lattice stability, band-gap modification, and reduction of defect states. The novelty of this study lies in directly contrasting Pb- and Sn-based mixed-halide systems under identical processing conditions, thereby revealing their complementary advantages and limitations. This comparison establishes $CH_3NH_3PbICl_2$ and $CH_3NH_3SnICl_2$ as promising candidates for stable, efficient, and environmentally more sustainable optoelectronic and photovoltaic applications.

2. Materials and Methods

2.1. Materials

Methylamine solution (CH_3NH_2, 40 wt.% in H_2O), hydroiodic acid (HI, 57%), diethyl ether, tin (II) chloride ($SnCl_2$), and lead (II) chloride ($PbCl_2$, 99.99%) were obtained from Karma Lab (Izmir, Turkey). Ethanol (≥99.9%), N, N-dimethylformamide (DMF, 99%), and dimethyl sulfoxide (DMSO, ≥99.7%) were purchased from Sigma-Aldrich. All chemicals were used without further purification.

2.2. Characterization Techniques

The structural, morphological, and optical properties of $CH_3NH_3SnICl_2$ and $CH_3NH_3PbICl_2$ perovskite thin films were examined using complementary characterization techniques. Surface morphology and film uniformity were studied by atomic force microscopy (AFM, NT-MDT) and optical microscopy (OM, Zeiss). Crystal structure was analyzed by X-ray diffraction (XRD, Rigaku MiniFlex) with Cu-Kα radiation (λ=1.5406 Å), scanned over a 2θ range of 20°-80° at a rate of 2°/min. Fourier-transform infrared spectroscopy (FTIR, PerkinElmer, USA) was employed to identify functional groups and vibrational modes in the 4000-400 cm^{-1} range. Optical absorption measurements were carried out using a Secord 250 Plus UV-Vis spectrophotometer, and photoluminescence (PL) spectra were recorded with a Cary Eclipse Varian fluorescence spectrophotometer.

2.2.1. Preparation of Perovskite Layers

Synthesis of Methylammonium Iodide (CH_3NH_3I). CH_3NH_3I was synthesized following a conventional acid-base neutralization route. Briefly, 20 mL of aqueous methylamine solution (CH_3NH_2, 40 wt.% in H_2O) was mixed with 60 mL of ethanol and cooled in an ice bath to 0 °C. Under continuous stirring 32 mL of hydroiodic acid (HI, 57%) was added dropwise, and the reaction was maintained for 2 h at 0 °C.

Subsequently, the mixture was then removed from the ice bath, and volatile components and excess solvents were evaporated under reduced pressure (~50 Torr) at 60 °C for 4 h. The resulting crude product was recrystallized from hot ethanol (~50 °C) and precipitated by adding 200 mL of anhydrous diethyl ether. The white crystalline solid was collected by filtration and dried under vacuum, producing CH_3NH_3I for perovskite precursor preparation.

Preparation of $CH_3NH_3SnICl_2$ Thin Films. To prepare $CH_3NH_3SnICl_2$, 0.19 g of synthesized CH_3NH_3I was dissolved in 0.5 mL of DMF to obtain a yellow solution. Separately, 0.42 g of $SnCl_2$ was dissolved in 0.5 mL of DMF under vigorous stirring. All solution processing steps were carried out under a nitrogen atmosphere to prevent oxidation of Sn^{2+} ions. The CH_3NH_3I solution was heated to 60 °C and magnetically stirred, after which the $SnCl_2$ solution was slowly added dropwise to ensure homogeneous mixing. The resulting mixture was stirred for 2 h to obtain a homogeneous perovskite precursor paste.

The prepared precursor was then deposited onto pre-cleaned glass substrates using the doctor-blade coating technique, followed by thermal annealing in a vacuum oven at 100 °C for 1 h to promote solvent evaporation, crystallization, and formation of the $CH_3NH_3SnICl_2$ perovskite phase.

Preparation of $CH_3NH_3PbICl_2$ Thin Films. For the preparation of $CH_3NH_3PbICl_2$ thin films, 0.18 g of synthesized CH_3NH_3I was dissolved in a solvent mixture of 0.4 mL DMF and 0.1 mL DMSO. Separately, 0.49 g of $PbCl_2$ was dissolved in the same DMF/DMSO solvent mixture under stirring. All solution processing steps were performed under a nitrogen atmosphere to suppress oxygen-induced degradation of the perovskite precursors. The $PbCl_2$ solution was slowly added dropwise to the CH_3NH_3I solution under continuous stirring at 60 °C, ensuring homogeneous mixing. The resulting precursor was stirred until homogeneous, complete dissolution and formation of a uniform, transparent perovskite ink.

The homogeneous precursor was subsequently deposited onto pre-cleaned glass substrates using the doctor-blade coating technique, followed by thermal annealing in a vacuum oven at 100 °C for 1 h to promote solvent evaporation, crystallization, and formation of the $CH_3NH_3PbICl_2$ perovskite phase. Thin films were deposited on glass substrates (Figure 1, a-b).

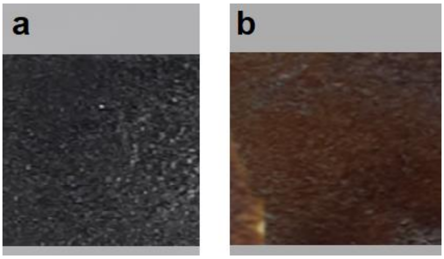

Fig. 1. Perovskite layers grown on glass substrates by the doctor-blade technique: (a) $CH_3NH_3PbICl_2$; (b) $CH_3NH_3SnICl_2$.

3. Results and Discussion

3.1. Optical Microscopy Analysis

The morphological features of $CH_3NH_3PbICl_2$ and $CH_3NH_3SnICl_2$ mixed-halide perovskite thin films were first examined by optical microscopy (Figure 2, a-b). Both $CH_3NH_3PbICl_2$ and $CH_3NH_3PbICl_2$ films exhibit uniform coverage and smooth surfaces, confirming controlled crystal growth and homogeneous film formation.

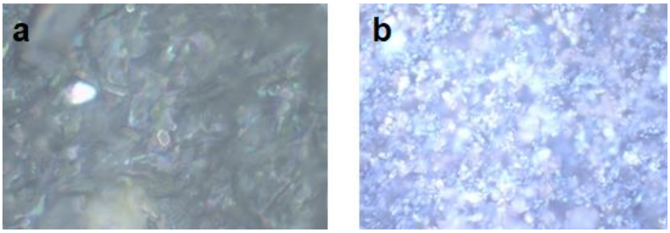

Fig. 2. Optical microscope images of perovskite films grown by the doctor blade technique: (a) $CH_3NH_3PbICl_2$; (b) $CH_3NH_3SnICl_2$.

The observed morphological uniformity indicates that partial substitution of iodide by chloride ions promotes developed film-forming ability, enhanced crystallization kinetics, and reduced macroscopic defects, which are essential for high-quality optoelectronic layers.

3.2. AFM Analysis

The surface topography and nanoscale morphology of the mixed-halide perovskite thin films were further examined by AFM (Figure 3, a-b). The $CH_3NH_3PbICl_2$

thin film has a granular microstructure and clearly defined grain boundaries, indicating a polycrystalline morphology with average grain sizes in the range of approx.-imately 150-300 nm.

In contrast, $CH_3NH_3SnICl_2$ thin films have smoother surface morphology with larger grains with sizes approximately 500-900 nm. The presence of enlarged crystalline domains and the decrease in grain boundary density points more efficient crystal growth and coalescence during film formation. Larger grains decrease the density of interfacial trap states and suppress non-radiative recombination, thereby enhancing charge transport and long-term structural stability.

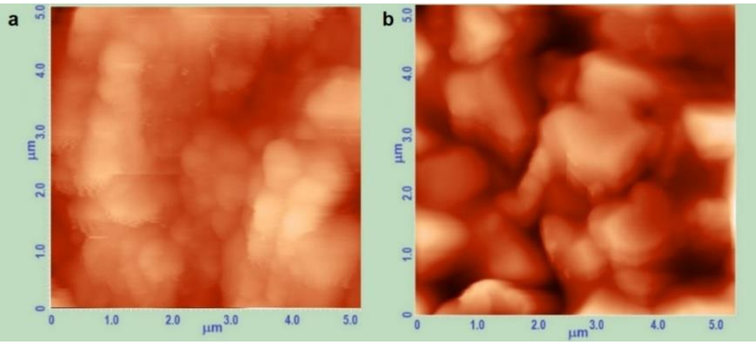

Fig. 3. 2D AFM images of perovskite films: (a) $CH_3NH_3PbICl_2$; (b) $CH_3NH_3SnICl_2$

Overall, in comparison with $CH_3NH_3PbICl_2$, the $CH_3NH_3SnICl_2$ films show increased crystallinity, lower surface roughness and reduced grain boundary density, making them more suitable for optoelectronic applications.

3.4. XRD Analysis of $CH_3NH_3PbICl_2$ and literature comparison with $CH_3NH_3SnICl_2$

Figure 4 demonstrates the XRD pattern of the $CH_3NH_3PbICl_2$ mixed-halide perovskite thin film. Phase identification was carried out using The Match! software in combination with the Crystallography Open Database (COD). The recorded diffraction peaks, their assigned crystallographic planes, and phase attributions are summarized in Table 1.

The diffraction results confirm the formation of well-crystallized $CH_3NH_3PbICl_2$, with dominant peaks at $2\theta \approx 14.04°$, 29.10°, and 43.90°, characteristic of the tetragonal mixed-halide perovskite phase. Secondary reflections at $2\theta \approx 15.51°$, 22.50°, and 31.42° indicate the presence of a cubic $CH_3NH_3PbCl_3$ phase, while weaker peaks at $2\theta \approx 35.18°$ and 39.12° indicate the presence of tetragonal $CH_3NH_3PbI_2Cl$ intermediate composition. Minor residual phases of PbI_2 and $PbCl_2$ were also observed, suggesting incomplete halide interdiffusion or slight precursor segregation during film formation.

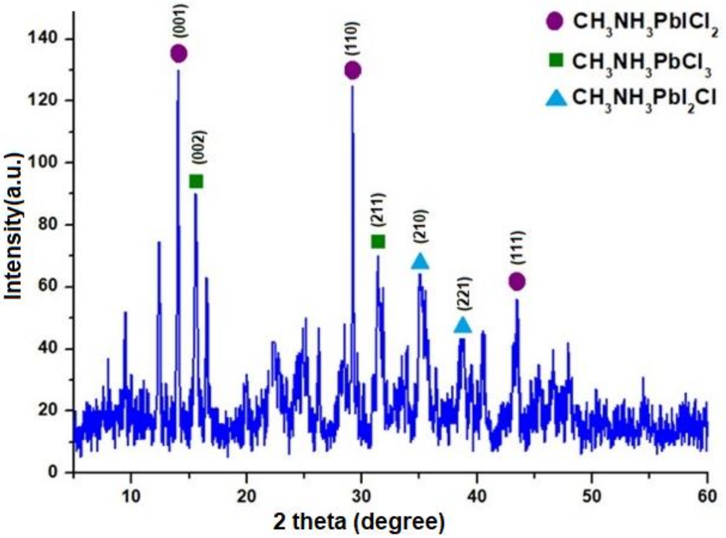

Fig. 4. XRD pattern of $CH_3NH_3PbICl_2$ perovskite thin film

Table 1. XRD diffraction peaks and phase attribution of $CH_3NH_3PbICl_2$ thin film

No	2θ (°)	Plane (hkl)	Phase Attribution
	12.38	(001)	PbI_2
	14.04	(001)	Tetragonal $CH_3NH_3PbICl_2$
	15.51	(002)	Cubic $CH_3NH_3PbCl_3$
	22.50	(110)	Cubic $CH_3NH_3PbCl_3$
	24.52	(021)	$PbCl_2$
	29.10	(110)	Tetragonal $CH_3NH_3PbICl_2$
	31.42	(211)	Cubic $CH_3NH_3PbCl_3$
	35.18	(210)	Tetragonal $CH_3NH_3PbI_2Cl$
	39.12	(221)	Tetragonal $CH_3NH_3PbI_2Cl$
	43.90	(111)	Tetragonal $CH_3NH_3PbICl_2$

Overall, $CH_3NH_3PbICl_2$ films are characterized by high crystallinity and good phase purity, which is favorable for optoelectronic applications [18-23].

Although direct experimental XRD data for $CH_3NH_3SnICl_2$ were not available in this study, literature reports indicate that tin-based mixed-halide perovskites exhibit similar tetragonal perovskite reflections near 2θ ≈ 14°, 28-29°, and 42°, consistent with a well-defined crystal structure [24-26]. However, in comparison with Pb-based analogues, the Sn-based films typically show broader diffraction peaks with reduced intensities, reflecting smaller crystallite sizes and partial structural disorder due to the intrinsic chemical instability of Sn^{2+} ions and their tendency toward oxidation to Sn^{4+}. Although chloride incorporation enhances crystallization, reduces defect formation, and enhances phase stability in both Pb- and Sn-based mixed-haled perovskites, the intrinsic instability of Sn^{2+} might the long-term structural durability of $CH_3NH_3SnICl_2$.

3.5. FTIR Analysis

The FTIR spectra of $CH_3NH_3PbICl_2$ and $CH_3NH_3SnICl_2$ thin films were analyzed molecular structure and lattice dynamics, with focus on the vibrational modes of the MA^+ cation and the effect of halide substitution. Both compounds display the characteristic MA^+ absorption manifold, whereas small but systematic shifts and bandwidth variations reflect differences in metal-halide bond polarizability, octahedral vibrational density of states, and $MA^+\cdots X$ (X=I/Cl) hydrogen-bond strength in the Pb- and Sn-based lattices [28-29]. Figure 5 shows the FTIR spectra of (a) $CH_3NH_3PbICl_2$ and (b) $CH_3NH_3SnICl_2$ thin films.

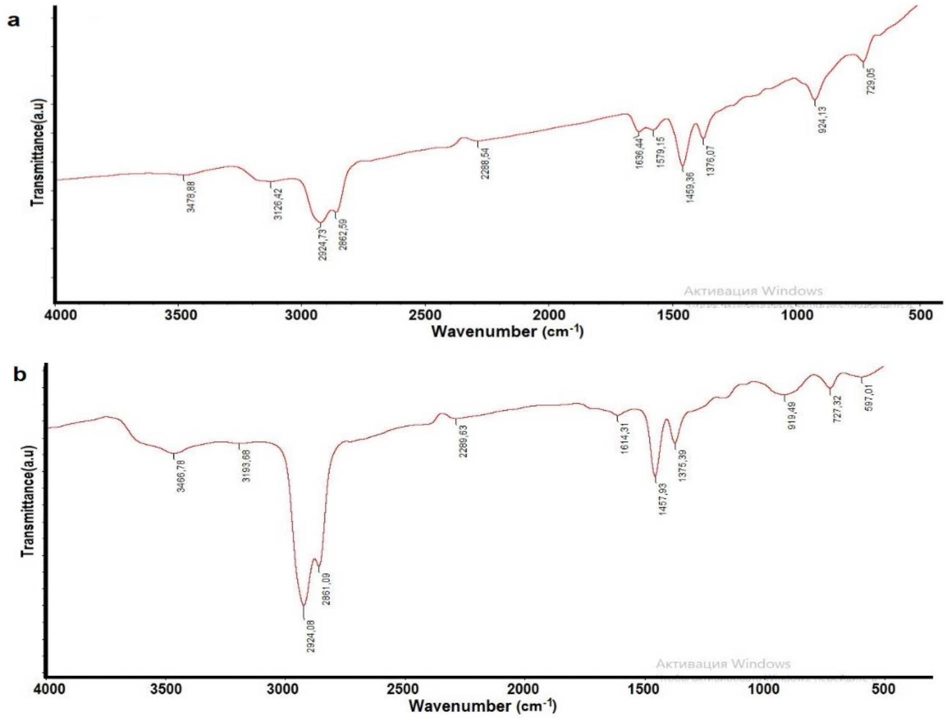

Fig. 5. FTIR images of perovskite thin films: (a) $CH_3NH_3PbICl_2$; (b) $CH_3NH_3SnICl_2$

In both spectra, broad absorptions near ~3466-3479 cm^{-1} correspond to O-H stretching, originating from surface water or hydrates, which is commonly observed for solution-processed perovskite films. Strong N-H stretching vibrations of the MA^+

cation occur between ~3126-3193 cm^{-1}, while symmetric and asymmetric C-H stretching modes are observed around 2861-2925 cm^{-1}.

N-H bending vibrations are detected around ~1614-1636 cm^{-1}, along with deformation modes of NH_3^+ (~1457-1459 cm^{-1}) and CH_3 bending (~1375-1376 cm^{-1}). Internal MA^+ cation vibrations are reflected by peaks at ~919-924 cm^{-1} (C-N stretching) and 727-729 cm^{-1}, commonly attributed to MA^+ hindered rotation that is sensitive to the inorganic cage potential [23, 29-31].

Furthermore, $CH_3NH_3SnICl_2$ displays an additional absorption band near ~597 cm^{-1}, corresponding to a lattice mode dominated by Sn-X (X=I/Cl) stretching/deformation within the SnX_6 octahedral framework. This feature, absent in $CH_3NH_3PbICl_2$, highlights the various lattice dynamics of the tin-based mixed-halide system. The comparative FTIR vibrational assignments of both perovskites are provided in Table 2.

Table 2. Comparative FTIR vibrational assignments of $CH_3NH_3PbICl_2$ and $CH_3NH_3SnICl_2$ perovskites

Wave number (cm^{-1})	Assignment	$CH_3NH_3PbICl_2$	$CH_3NH_3SnICl_2$	Notes
3466-3479	O-H stretching	✓	✓	Adsorbed surface moisture/hydrate-like species; may partially overlap with high-frequency N-H modes
3126-3193	N-H stretching (MA^+)	✓	✓	Highly sensitive to $MA^+\cdots X$ (X=I, Cl) hydrogen bonding and local lattice distortion
2861-2863, 2924-2925	C-H stretching	✓	✓	Symmetric and asymmetric CH_3 vibrations; weakly affected by B-site substitution
1614-1636	N-H bending	✓	✓	May overlap with H-O-H bending of residual water; position reflects hydrogen-bond strength
1457-1459	NH_3^+ deformation	✓	✓	Strong coupling with inorganic cage potential and MA^+ orientation
1375-1376	CH_3 bending	✓	✓	Internal MA^+ mode; weak sensitivity to halide substitution
919-924	C-N stretching	✓	✓	Characteristic internal vibration of MA^+ cation
727-729	MA^+ (hindered rotation)	✓	✓	Sensitive to dynamic disorder and octahedral cage symmetry
~597	Sn-X (X=I, Cl) lattice deformation mode	–	✓	Low-frequency framework vibration specific to Sn-based perovskite; reflects modified octahedral dynamics rather than “stability”

Overall, FTIR confirms that both $CH_3NH_3PbICl_2$ and $CH_3NH_3SnICl2$ retain the full MA^+ vibrational fingerprint, while $Pb^{2+}\rightarrow Sn^{2+}$ substitution and mixed-halide coordination introduce measurable perturbations in band positions and linewidths, consistent with modified hydrogen bonding, dynamic disorder, and inorganic cage vibrations. The additional ~597 cm^{-1} lattice feature in the Sn-based film indicates a distinct octahedral vibrational contribution associated with Sn-X bonding, highlighting the sensitivity of mixed-halide perovskite lattice dynamics to B-site chemistry.

3.6. Absorption Properties and Band Gap Analysis

Hybrid organo-inorganic perovskites exhibit outstanding optoelectronic properties, including direct band gap electronic structure, high absorption coefficients ($\alpha \approx 10^4$-10^5 cm^{-1} near the band edge), and the ability to modifying optical properties via halide composition. These characteristics make them excellent candidates for high-efficiency and lightweight solar cells, photodetectors, and other optoelectronic devices. However, their long-term stability remains limited due to sensitivity to moisture, oxygen, and thermal fluctuations. Partial halide substitution, particularly the incorporation of Cl^- into iodide-based frameworks, is widely adopted strategy to improve structural stability, reduce defect density, and modulate the electronic structure.

The UV-Vis absorption spectra of $CH_3NH_3PbICl_2$ and $CH_3NH_3SnICl_2$ thin films, along with their corresponding Tauc plots, are presented in Figure 6 and Figure 7, respectively.

Figure 6(a) illustrates a well-defined absorption edge around ~760 nm, characteristic of a direct band gap transition with excitonic features. Compared with pure $CH_3NH_3PbI_3$, this band edge is blue-shifted due to partial replacement of I^- by more electronegative Cl^- ions, resulting in lattice distortion and band gap widening. The broader absorption edge and reduced Urbach tail also indicates enhanced crystallinity and lower defect density. The optical band gap, calculated from the Tauc plot (Figure 6(b)), was calculated to be $E_g \approx 1.54$ eV, reliable with reported values for mixed-halide lead perovskites [29, 32, 33].

The absorption spectrum of $CH_3NH_3SnICl_2$ (Figure 7(a)) shows a beginning, g near 830 nm, extending across the 820-880 nm the near-infrared region, consistent with the narrower band gap characteristic of Sn-based perovskites. Compared to $CH_3NH_3SnI_3$ ($E_g \approx 1.35$ eV), the Cl^- incorporation induces a clear blue-shift of the absorption edge and a slightly wider band gap of $E_g \approx 1.55$ eV, as estimated from the Tauc plot (Figure 7(b)). The sharper absorption edge also represents improved structural order and reduced recombination pathways, confirming the advantage of chloride substitution on the optoelectronic quality of the films [34].

Overall, both Pb- and Sn-based mixed-halide perovskites demonstrate band gap widening and sharpening of the absorption edges upon partial Cl^- incorporation,

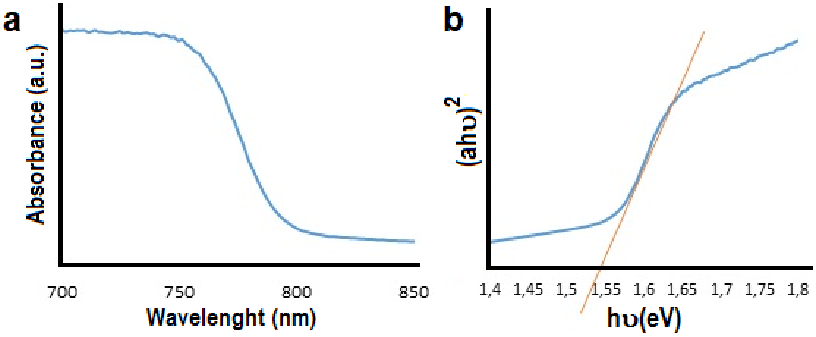

Fig. 6. UV-Vis absorption and band gap analysis of mixed-halide $CH_3NH_3PbICl_2$ perovskite thin films: (a) absorption spectrum of thin film; (b) Tauc plot of $CH_3NH_3PbICl_2$ thin film showing the direct band gap (Eg≈1.54 eV)

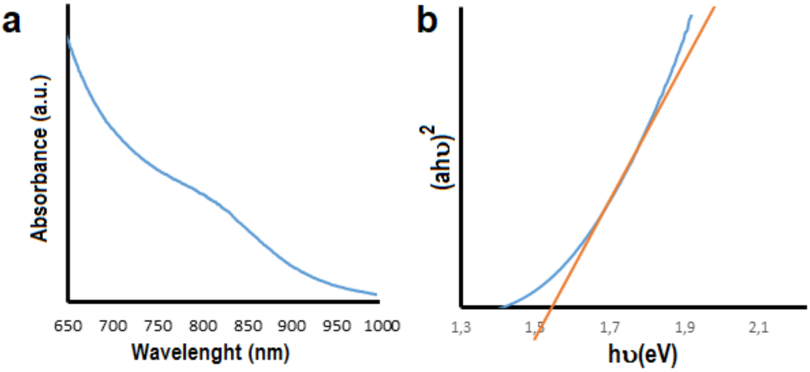

Fig. 7. UV-Vis absorption and band gap analysis of mixed-halide $CH_3NH_3SnICl_2$ perovskite thin films: (a) absorption spectrum of thin film; (b) Tauc plot of $CH_3NH_3SnICl_2$ showing the direct band gap (Eg≈1.55 eV)

highlighting the stabilizing role of halide mixing. These minor differences among $CH_3NH_3PbICl_2$ and $CH_3NH_3SnICl_2$ originate from the distinct electronic configurations of Pb^{2+} ($6s^2$) and Sn^{2+} ($5s^2$) cations and their different degrees of s-p antibonding interaction with halide orbitals. Nevertheless, both systems benefit from partial chloride-induced improvements in crystallinity, reduced defect density, and optical tunability, which are crucial parameters for advancing next-generation perovskite optoelectronic devices.

3.7. PL Analysis

PL spectroscopy is a sensitive, non-destructive method to assess the crystallinity, defect states, and recombination dynamics in hybrid perovskite films.

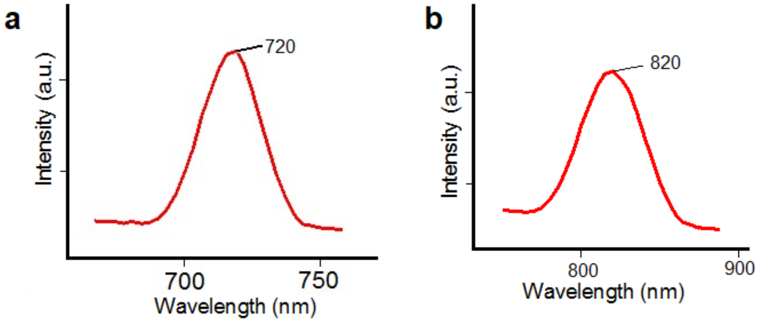

Fig. 8. Photoluminescence spectra of mixed-halide perovskite thin films: (a) $CH_3NH_3PbICl_2$; (b) $CH_3NH_3SnICl_2$

The PL spectra of $CH_3NH_3PbICl_2$, recorded under 500 nm excitation at room temperature (Figure 8(a)), reveals a sharp and symmetric emission peak centered at ~720 nm. The narrow emission profile suggests effective radiative recombination, a low density of non-radiative defect states, and high crystallinity of the film. The partial incorporation of Cl^- ions improves film morphology and reduces trap states, leading to improved PL intensity and spectral sharpness. The observed blue shift relative to $CH_3NH_3PbI_3$ is attributed to bandgap widening induced by lattice contraction, modified Pb-X orbital overlap, and altered $MA^+\cdots X$ hydrogen bonding (including C-N···Cl interactions). Furthermore, analyses reveal that Cl^- segregation across grains can affect local emission behavior, resulting in slight PL shifts [25, 35].

The PL spectrum of $CH_3NH_3SnICl_2$ thin films (Figure 8(b)) exhibits a pronounced emission peak at ~820 nm, associated with its direct band gap and near-infrared emission properties. The sharpness and symmetry of the peak indicates enhanced film crystallinity and minimized defect-mediated non-radiative recombination. Incorporation of Cl^- ions into the Sn-I framework is known to retard Sn^{2+} oxidation, leads to improved structural order and more efficient radiative efficiency, yielding stronger PL emission compared to pure $CH_3NH_3SnI_3$. Compared with pure $CH_3NH_3SnI_3$, the emission peak is blue-shifted, consistent with chloride-induced widening of the electronic band gap in agreement with UV-Vis and Tauc analyses [13, 23, 36].

Overall, chloride incorporation in both Pb- and Sn-based mixed-halide perovskites improves PL by stabilizing the lattice, reducing non-radiative losses, and enhancing optical quality, making them more appropriate for photovoltaic and photonic applications.

The combined PL and UV-Vis results consistently show the band gap tuning through controlled halide substitution enhances crystallinity, suppresses defect-related recombination, and strengthens both absorption and emission features, confirming that mixed-halide engineering is an effective strategy for optimizing overall optical performance of perovskite absorbers and emitters.

4. Conclusion

This study examined the structural and optical features of mixed-halide hybrid perovskite thin films, $CH_3NH_3SnICl_2$ and $CH_3NH_3PbICl_2$, with particular attention to the role of partial iodide-to-chloride substitution in boosting material performance. For $CH_3NH_3PbICl_2$, XRD analysis verified the formation of a mainly tetragonal perovskite phase, along with minor contributions from cubic $CH_3NH_3PbCl_3$. The presence of secondary phases of PbI_2 and $PbCl_2$ were detected, suggesting partial phase instability and response to degradation in ambient conditions, highlighting the metastable nature of mixed-halide lead perovskites under environmental exposure.

The FTIR spectra showed the characteristic vibrational modes of the organic $CH_3NH_3^+$ cation, supporting the hybrid framework. Optical absorption measurements revealed a sharp absorption edge at ~760 nm and a direct band gap of $Eg \approx 1.54$ eV, consistent with chloride-induced bandgap widening. The PL spectrum showed a strong, narrow emission peak at 750 nm, confirming high crystallinity and low non-radiative recombination. Nevertheless, the detection of secondary phases highlights the necessity for further optimization of synthesis protocols to improve phase purity and long-term stability.

In contrast, $CH_3NH_3SnICl_2$ thin films showed increased structural integrity upon Cl^- incorporation. XRD and AFM data revealed larger grain size and higher crystallinity, while FTIR spectra confirmed characteristic $CH_3NH_3^+$ vibrational modes with slight shifts indicating modified lattice interactions. UV-Vis analysis revealed a band gap of $Eg \approx 1.55$ eV with strong absorption near 830 nm. PL spectra revealed a sharp emission peak in the near-infrared region at ~820 nm, blue-shifted relative to pure $CH_3NH_3SnI_3$, indicating reduced defect density and improved crystal quality. Importantly, the absence of pronounced secondary phases suggests more homogeneous halide incorporation and potentially enhanced structural stability in the Sn-based mixed-halide system.

Overall, both Pb- and Sn-based mixed-halide perovskites show that partial I^- replacement with Cl^- improves optical band gap, crystallinity, and suppresses non-radiative recombination pathways. While $CH_3NH_3PbICl_2$, has strong optical absorption and efficient emission, its tendency to secondary-phase formation highlights persistent stability challenges. Conversely, $CH_3NH_3SnICl_2$ has desirable band gap tunability, high PL intensity, and better structural quality, making it a viable choice for photovoltaic and optoelectronic applications.

In conclusion, chloride partial integration is an effective strategy for stabilizing the perovskite lattice, improving optoelectronic quality, and modulating band gap features. Although Pb-based perovskites remain high-performing but stability-limi-ted, Sn-based mixed-halide analogs such as $CH_3NH_3SnICl_2$ provide significant potential for developing ecologically friendly, efficient, and stable next-generation perovskites.

References

[1] Stoumpos, C. C.; Malliakas, C. D.; Kanatzidis, M. G. Semiconducting tin and lead iodide perovskites with organic cations: Phase transitions, high mobilities, and near infrared photoluminescent properties. *Inorg. Chem.* **2013**, 52, pp. 9019–9038, DOI: 10.1021/ic401215x

[2] Tao, S.; Schmidt, I.; Brocks, G.; Jiang, J.; Tranca, I.; Meerholz, K.; Olthof, S. Absolute energy level positions in tin- and lead-based halide perovskites. *Nat. Commun.* **2019**, 10, 2560, DOI: 10.1038/s41467-019-10468-7

[3] Cho, A.; Park, N. Impact of interfacial layers in perovskite solar cells. *ChemSusChem* **2017**, 10, pp. 3687–3704, DOI: 10.1002/cssc.201701095

[4] Ghasemi, M.; Hao, M.; Xiao, M.; Chen, P.; He, D.; Zhang, Y.; Chen, W.; Fan, J.; Yun, J. H.; Jia, B.; Wen, X. Lead-free metal-halide double perovskites: From optoelectronic properties to applications. *Nanophotonics* **2021**, 10, pp. 2181–2219, DOI: 10.1515/nanoph-2020-0548

[5] Liu, M.; Grandhi, G. K.; Matta, S.; Mokurala, K.; Litvin, A.; Russo, S.; Vivo, P. Halide perovskite nanocrystal emitters. *Adv. Photon. Res.* **2021**, 2, 2000118, DOI: 10.1002/adpr.202000118

[6] Moyez, S. A.; Roy, S. Thermal engineering of lead-free nanostructured $CH_3NH_3SnCl_3$ perovskite material for thin-film solar cells. *J. Nanopart. Res.* **2017**, 20, pp. 1–12, DOI: 10.1007/s11051-017-4108-z

[7] Shamsi, J.; Urban, A. S.; Imran, M.; De Trizio, L.; Manna, L. Metal halide perovskite nanocrystals: Synthesis, post-synthesis modifications, and their optical properties. *Chem. Rev.* **2019**, 119, pp. 3296–3348, DOI: 10.1021/acs.chemrev.8b00644

[8] Hu, L.; Zhao, W.; Duan, W.; Chen, G.; Fan, B.; Zhang, X. Temperature-dependent optical properties of perovskite quantum dots with mixed A-cations. *Micromachines* **2022**, 13, 457, DOI: 10.3390/mi13030457

[9] Protesescu, L.; Yakunin, S.; Bodnarchuk, M. I.; Krieg, F.; Caputo, R.; Hendon, C. H.; Yang, R. X.; Walsh, A.; Kovalenko, M. V. Nanocrystals of cesium lead halide perovskites ($CsPbX_3$, X = Cl, Br, and I): Novel optoelectronic materials showing bright emission with wide color gamut. *Nano Lett.* **2015**, 15, pp. 3692–3696, DOI: 10.1021/nl5048779

[10] Prabhakaran, A.; Dhanabalan, B.; Andrusenko, I.; Pianetti, A.; Lauciello, S.; Prato, M.; Marras, S.; Solokha, P.; Gemmi, M.; Brovelli, S.; Manna, L.; Arciniegas, M. P. Stable Sn-based hybrid perovskite-related structures with tunable color coordinates via organic cations in low-temperature synthesis. *ACS Energy Lett.* **2023**, 8, pp. 2630–2640, DOI: 10.1021/acsenergylett.3c00791

[11] Karim, A. M. M. T.; Hossain, M. S.; Khan, M. K. R.; Kamruzzaman, M.; Rahman, M. A.; Rahman, M. M. Solution-processed mixed halide $CH_3NH_3PbI_{3-x}Cl_x$ thin films prepared by repeated dip coating. *J. Mater. Sci.* **2019**, 54, pp. 11818–11826, DOI: 10.1007/s10853-019-03740-0

[12] Bouich, A.; Marí-Guaita, J.; Soucase, B. M.; Palacios, P. Manufacture of high-efficiency

and stable lead-free solar cells through antisolvent quenching engineering. *Nanomaterials* **2022**, 12, 2901, DOI: 10.3390/nano12172901

[13] Ananthajothi; Venkatachalam, S. Synthesis and optical characterization of CdS, CdSe quantum dots and $CH_3NH_3SnCl_3$ perovskite sensitizers used in solar cell applications. *Int. J. Recent Sci. Res.* **2015**, 6, pp. 6640–6644

[14] Lu, P.; Lu, M.; Wang, H.; Sui, N.; Shi, Z.; Yu, W. W.; Zhang, Y. Metal halide perovskite nanocrystals and their applications in optoelectronic devices. *InfoMat* **2019**, 1, pp. 430–459, DOI: 10.1002/inf2.12031

[15] Feng, J.; Xiao, B. Effective masses and electronic and optical properties of non-toxic $MASnX_3$ (X = Cl, Br, and I) perovskite structures as solar cell absorbers: A theoretical study. *J. Phys. Chem. C* **2014**, 118, pp. 19655–19660, DOI: 10.1021/jp506498k

[16] Arzefooni, A. A.; Izadifard, M.; Ghazi, M.; Pour, F. A. Study of structural, optical, and electrical properties of $MA(FA)SnICl_2$ perovskite thin films synthesized by one-step spin coating. *Iran. J. Crystallogr. Mineral.* **2021**, 29, pp. 919–932, DOI: 10.52547/ijcm.29.4.919

[17] Zhang, F.; Ma, Z.; Shi, Z.; Chen, X.; Wu, D.; Li, X.; Shan, C. Recent advances and opportunities of lead-free perovskite nanocrystals for optoelectronic applications. *Energy Mater. Adv.* **2021**, 2021, 5198145, DOI: 10.34133/2021/5198145

[18] Fatema, K.; Ahmed, M. T.; Hossain, M. K.; Ahmed, F. Structural and morphological properties of single and mixed halide Pb-based perovskites. *Adv. Condens. Matter Phys.* **2022**, 2022, 6001569, DOI: 10.1155/2022/6001569

[19] Zhang, Z. L.; Men, B. Q.; Liu, Y. F.; Gao, H. P.; Mao, Y. L. Effects of precursor solution composition on the performance and I–V hysteresis of perovskite solar cells based on $CH_3NH_3PbI_{3-x}Cl_x$. *Nanoscale Res. Lett.* **2017**, 12, 343, DOI: 10.1186/s11671-017-1872-8

[20] Chigari, S. S.; Chavan, V. C.; Farasani, S. M.; Bhosale, V. K.; Ravikumar, A. Ultrasonic radiation assisted synthesis of $(CH_3NH_3)_2CuCl_4$, $CH_3NH_3PbCl_3$, and $CH_3NH_3SnCl_3$ perovskites for energy applications. *J. Hazard. Mater. Adv.* **2023**, 12, 100368, DOI: 10.1016/j.hazadv.2023.100368

[21] Wei, P.; Tseng, Y.; Tseng, H.; Wu, S.; Hu, J.; Yung, T.; Chen, T.; Wu, H.; Wu, C.; Li, W. Thermally sensitive infrared absorption bands and lattice incommensurability in photoelectric $CH_3NH_3PbI_3$. *Phys. Rev. Mater.* **2025**, 9, 055401, DOI: 10.1103/PhysRevMaterials.9.055401

[22] Tseng, Y.; Tseng, Y.; Wu, C. Photovoltaic performance of $CH_3NH_3PbI_2Cl$ perovskite solar cells. *Appl. Funct. Mater.* **2022**, 2, pp. 14–20, DOI: 10.35745/afm2022v02.02.0003

[23] Liu, J.; Xue, Y.; Wang, Z.; Xu, Z.; Zheng, C.; Weber, B.; Song, J.; Wang, Y.; Lu, Y.; Zhang, Y.; Bao, Q. Two-dimensional $CH_3NH_3PbI_3$ perovskite: Synthesis and optoelectronic applications. *ACS Nano* **2016**, 10, pp. 3536–3542, DOI: 10.1021/acsnano.5b07791

[24] Mitzi, D. B.; Liang, K. Synthesis, resistivity, and thermal properties of the cubic perovskite $NH_2CH{=}NH_2SnI_3$ and related systems. *J. Solid State Chem.* **1997**, 134, pp. 376–381, DOI: 10.1006/jssc.1997.7593

[25] Bao, X.; Mu, H.; Chen, Y.; Li, P.; Li, L.; Li, S.; Qasim, K.; Zhang, Y.; Zhang, H.; Bao, Q.

Ytterbium-doped fiber laser passively mode locked by evanescent field interaction with $CH_3NH_3SnI_3$ perovskite saturable absorber. *J. Phys. D: Appl. Phys.* **2018**, 51, 375106, DOI: 10.1088/1361-6463/aad71d

[26] Huang, Y.; Su, J.; Li, Q.; Wang, D.; Xu, L.; Bai, Y. Structure, optical and electrical properties of $CH_3NH_3SnI_3$ single crystals. *Physica B* **2019**, 563, pp. 107–112, DOI: 10.1016/j.physb.2019.03.035

[27] Xia, H.; Sun, W.; Peng, L. Hydrothermal synthesis of organometal halide perovskites for Li-ion batteries. *Chem. Commun.* **2015**, 51, pp. 13787–13790, DOI: 10.1039/C5CC05053G

[28] Badrooj, M.; Jamali-Sheini, F.; Torabi, N. Optoelectronic properties of mixed Sn/Pb perovskite solar cells: The study of compressive strain by Raman modes. *J. Phys. Chem. C* **2020**, 124, pp. 27136–27147, DOI: 10.1021/acs.jpcc.0c07999

[29] Matheu, R.; Vigil, J. A.; Crace, E. J.; Karunadasa, H. I. The halogen chemistry of halide perovskites. *Trends Chem.* **2022**, 4, pp. 206–219, DOI: 10.1016/j.trechm.2021.12.002

[30] Noorlaily, P.; Ulfa, M.; Bisri, S. Z.; Iskandar, F. Absorbance studies of perovskite $CH_3NH_3PbI_{3-x}Cl_x$ as light harvester in solar cells. *Adv. Mater. Res.* **2015**, 1112, pp. 282–285, DOI: 10.4028/www.scientific.net/AMR.1112.282

[31] Patel, J. B.; Milot, R. L.; Wright, A. D.; Herz, L. M.; Johnston, M. B. Formation dynamics of $CH_3NH_3PbI_3$ perovskite following two-step layer deposition. *J. Phys. Chem. Lett.* **2016**, 7, pp. 96–102, DOI: 10.1021/acs.jpclett.5b02495

[32] Gopinathan, N.; Basha, S. S.; Banu, I. B. S.; Mamat, M. H.; Sirajudeen, M. M. S. Solvents driven structural, morphological, optical, and dielectric properties of lead-free perovskite $CH_3NH_3SnCl_3$ for optoelectronic applications: Experimental and DFT study. *Mater. Res. Express* **2019**, 6, 125921, DOI: 10.1088/2053-1591/ab6a47

[33] Sengodan, S.; Choi, S.; Jun, A.; Shin, T. H.; Ju, Y.; Jeong, H. Y.; Shin, J.; Irvine, J. T. S.; Kim, G. Layered oxygen-deficient double perovskite as an efficient and stable anode for direct hydrocarbon solid oxide fuel cells. *Nat. Mater.* **2015**, 14, pp. 205–209, DOI: 10.1038/nmat4166

[34] Huang, F.; Pascoe, A. R.; Wu, W.; Ku, Z.; Peng, Y.; Zhong, J.; Caruso, R. A.; Cheng, Y.-B. Effect of the microstructure of the functional layers on the efficiency of perovskite solar cells. *Adv. Mater.* **2017**, 29, 1601715, DOI: 10.1002/adma.201601715

[35] Guo, X.; Burda, C. Coordination engineering toward high performance organic–inorganic hybrid perovskites. *Coord. Chem. Rev.* **2016**, 320–321, pp. 53–65, DOI: 10.1016/j.ccr.2016.03.013

[36] Guo, J.; Fu, Y.; Lu, M.; Zhang, X.; Kershaw, S. V.; Zhang, J.; Luo, S.; Li, Y.; Yu, W. W.; Rogach, A. L.; Zhang, L.; Bai, X. Cd-rich alloyed $CsPb_{1-x}Cd_xBr_3$ perovskite nanorods with tunable blue emission and Fermi levels fabricated through crystal phase engineering. *Adv. Sci.* **2020**, 7, 2000930, DOI: 10.1002/advs.202000930